Understanding ENSO dynamics through the exploration of past climates

Steven J. Phipps[1] and Jaclyn N. Brown[2]

[1]Climate Change Research Centre, University of New South Wales, Sydney, Australia (s.phipps@unsw.edu.au)
[2]Centre for Australian Weather and Climate Research, Hobart, Tasmania, Australia

1. Introduction

Proxy reconstructions from across the Pacific Basin (e.g. Rodbell et al., 1999) indicate that significant changes in ENSO characteristics took place during the Holocene. "Modern" El Niño variability began around 7–5 ka BP, with only weak decadal-scale events occurring beforehand. ENSO was 15–60% weaker at 6 ka than at present, with a gradual strengthening thereafter. There is also evidence of a peak in variability at 2–1 ka.

The climate system models that participated in Phase 2 of the Paleoclimate Modelling Intercomparison Project (PMIP2) simulated El Niño amplitudes that were 2.9–23% weaker at 6 ka than at present (Zheng et al., 2008). A consistent mechanism was found to apply across all the models, with insolation changes enhancing the seasonal cycle in the Northern Hemisphere. This intensified the Asian summer monsoon system, increasing the strength of the easterly trade winds in the central and western Pacific. These enhanced trade winds acted to suppress the development of El Niño events.

Here, we use a climate system model to simulate the orbitally-driven changes in the global climate over the past 8,000 years. The simulations are used to explore the links between ENSO dynamics and global climate change.

2. Climate model simulations

We use the CSIRO Mk3L climate system model v1.1 (Phipps, 2006). It comprises an atmospheric general circulation model with a resolution of 5.6°×3.2° and 18 vertical levels, an oceanic general circulation model with a resolution of 2.8°×1.6° and 21 vertical levels, a dynamic-thermodynamic sea ice model, and a land surface scheme with static vegetation.

Equilibrium simulations are conducted for 8, 7, 6, 5, 4, 3, 2, 1 and 0 ka BP. These are idealised experiments, in that *only* the Earth's orbital geometry is varied. Otherwise, the model is configured for pre-industrial conditions, with an atmospheric CO_2 concentration of 280 ppm and a solar constant of 1365 Wm^{-2}. Each experiment is integrated for 1000 years under constant boundary conditions.

Figure 1 shows the standard deviations of the simulated Niño 3 and Niño 3.4 SST anomalies. The model is able to reproduce the trends in ENSO variability over the past 8,000 years, with a gradual increase in strength and a statistically-significant peak at 1 ka. Based on variability in the Niño 3.4 region, the amplitude of El Niño is 16% weaker at 6 ka than at present. This is consistent with the PMIP2 models, and within the range of uncertainty in the reconstructions. We therefore conclude that the model is a useful tool for exploring changes in ENSO behaviour.

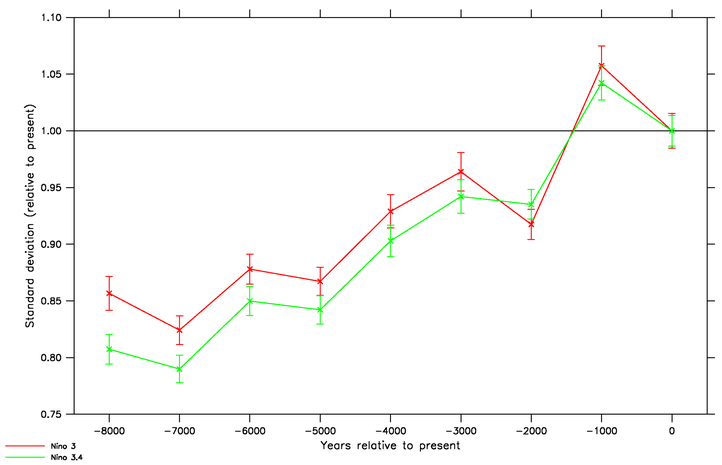

Figure 1. The normalised standard deviations of the monthly Niño 3 (red) and Niño 3.4 (green) sea surface temperature anomalies. The 95% confidence intervals are shown.

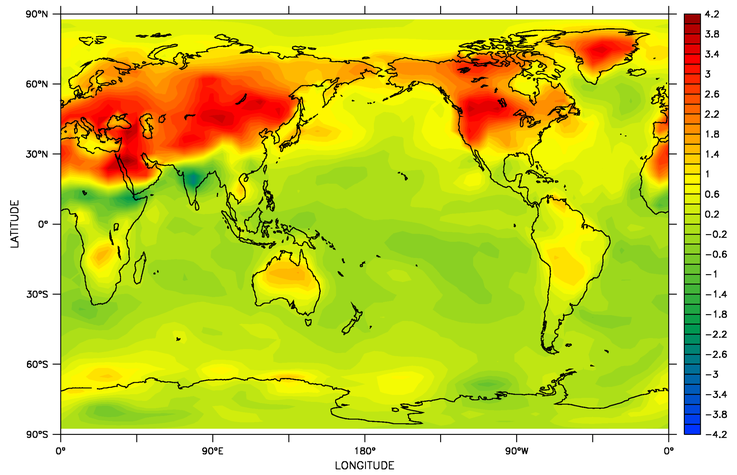

Figure 2. June-July-August surface air temperature, 8 ka minus 0 ka BP (K).

3. ENSO dynamics and global climate change

We now use the model simulations to explore the links between ENSO dynamics and the global climate. Figure 2 shows the difference in the June-July-August surface air temperature between the 0 ka and 8 ka simulations. Enhanced insolation at mid- and high northern latitudes at 8 ka results in temperatures over land that are up to 4 K higher than at present. However, because the oceans have a much larger heat capacity than the land, the magnitude of the changes over the ocean is smaller.

The increased land-sea temperature contrast leads to a dramatic intensification of the Asian summer monsoon system, as can be seen in Figure 3. The mean sea level pressure over the Eurasian and African landmasses is reduced by up to 6 hPa, with the enhanced deep convection drawing increased inflows of air from the tropical Pacific and Indian Oceans. The Walker Circulation over the Pacific Ocean is intensified, with an increase in the strength of the easterly trade winds in the central and western Pacific.

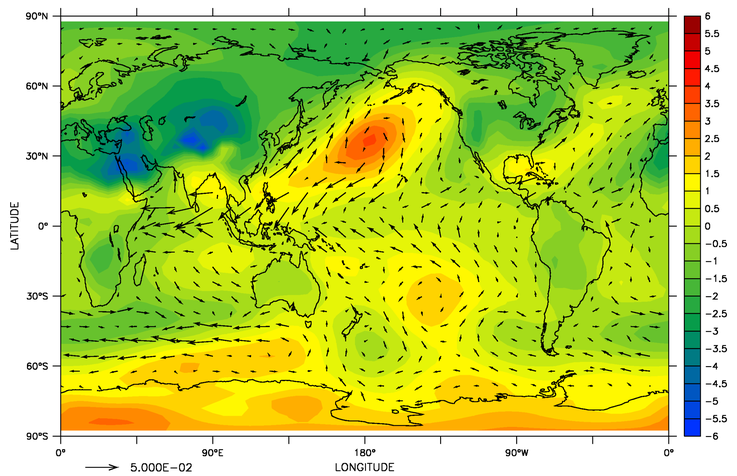

Figure 3. June-July-August atmospheric circulation, 8 ka minus 0 ka BP: mean sea level pressure (hPa; shading), and surface wind stress over the ocean (Nm^{-2}; vectors).

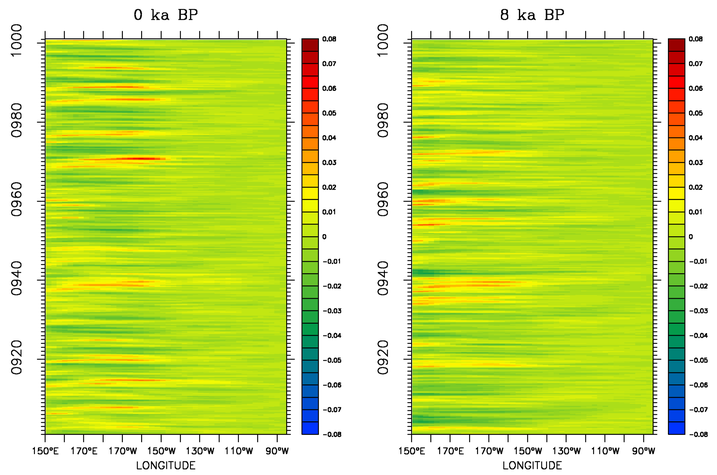

Figure 4. Monthly zonal wind stress anomalies at the equator, 0 ka and 8 ka BP (Nm^{-2}). The values shown are the five-month running means of the anomalies for the final 100 years of each simulation.

The intensification of the Walker Circulation changes the susceptibility of the coupled atmosphere-ocean system to the initiation of El Niño events. Figure 4 shows the propagation of westerly wind bursts within the 0 ka and 8 ka simulations. At 0 ka, most of the wind bursts propagate eastwards and are able to trigger El Niño events. At 8 ka, however, the stronger easterly trade winds act as a barrier. Many of the wind bursts are confined to the western Pacific, inhibiting the onset of El Niño events.

The same mechanism is found to operate across all the simulations (not shown). As the summer insolation at northern mid-latitudes decreases from 8 ka to 0 ka, the Asian summer monsoon system and Walker Circulation weaken. The tropical Pacific therefore becomes increasingly susceptibile to the initiation of El Niño events. While this mechanism explains the upward trend in ENSO variability over the past 8,000 years, however, it does not account for the simulated peak at 1 ka.

4. Conclusions

By forcing a climate system model with orbitally-driven insolation changes, we have been able to reproduce the trends in ENSO variability over the past 8,000 years.

Decreasing summer insolation over this period has resulted in a weakening of the Asian summer monsoon system. This has reduced the stability of the background state of the tropical Pacific, making it easier for El Niño events to develop. While this mechanism has previously been shown to explain the weaker ENSO at 6 ka, we have shown here that it is able to explain the upward trend in ENSO variability over the past 8,000 years. However, other mechanisms also appear be at work.

A full understanding of the processes that drive changes in ENSO variability may be within grasp. However, this will require an approach that integrates the data, modelling and theory communities.

5. References

Phipps, S. J. (2006), The CSIRO Mk3L Climate System Model, *Technical Report No. 3*, Antarctic Climate & Ecosystems Cooperative Research Centre, Hobart, Tasmania, Australia, 236 pp., ISBN 1-921197-03-X.

Rodbell, D. T., G. O. Seltzer, D. M. Anderson, M. B. Abbott, D. B. Enfield and J. H. Newman (1999), An ∼15,000-Year Record of El Niño–Driven Alluviation in Southwestern Ecuador, *Science*, *283*, 516–520.

Zheng, W., P. Braconnot, E. Guilyardi, U. Merkel and Y. Yu (2008), ENSO at 6ka and 21ka from ocean-atmosphere coupled model simulations, *Climate Dynamics*, *30*, 745–762.

Acknowledgements: Steven Phipps would like to thank the ARC Research Network for Earth System Science and the Australasian Quaternary Association for travel support.